Effects of an endothermic phase transition at 670 km depth in a spherical model of convection in the Earth's mantle

Paul J. Tackley*, David J. Stevenson†, Gary A. Glatzmaier‡ & Gerald Schubert§

* Seismological Laboratory, California Institute of Technology, Pasadena, California 91125, USA
† Division of Geological and Planetary Sciences, California Institute of Technology, Pasadena, California 91125, USA
‡ Earth and Environmental Sciences Division and Institute of Geophysics and Planetary Physics, Los Alamos National Laboratory, Los Alamos, New Mexico 87545, USA
§ Department of Earth and Space Sciences and Institute of Geophysics and Planetary Physics, University of California, Los Angeles, California 90024, USA

Numerical modelling of mantle convection in a spherical shell with an endothermic phase change at 670 km depth reveals an inherently three-dimensional flow pattern, containing cylindrical plumes and linear sheets which behave differently in their ability to penetrate the phase change. The dynamics are dominated by accumulation of downwelling cold material above 670 km depth, resulting in frequent avalanches of upper-mantle material into the lower mantle. This process generates long-wavelength lateral heterogeneity, helping to resolve the contradiction between seismic tomographic observations and expectations from mantle convection simulations.

THE question of whether an endothermic phase transition associated with the seismic discontinuity at 670 km depth could enforce layered convection in the Earth's mantle has received much attention[1-5], and has profound implications for the Earth's thermal and chemical structure and evolution[6]. Early two-dimensional numerical modelling[1] seemed to show that an unrealistically large Clapeyron slope of -6 MPa K^{-1} would be required for layering to occur. Recent work in two-dimensional cartesian[2,3,48] and spherical axisymmetric[4,5] geometries with realistic phase-change parameters has, however, indicated significant layering, as well as complex new phenomena and modes of time-dependence in the flow.

To understand the Earth it is essential to determine how the effects observed in these two-dimensional studies are modified in three-dimensional geometry. Here we present results from a numerical simulation of fully three-dimensional compressible mantle convection in a spherical shell with an endothermic phase change at 670 km depth. The spatial resolution and Rayleigh number are much higher than in previous spherical models with no phase change[7-9]. Although there are some similarities with the two-dimensional results, the simulated flow pattern is inherently three-dimensional, with features that penetrate the phase change being exclusively cylindrical in form. The upper mantle is characterized by interconnected linear downwellings which do not penetrate. At the intersections of these downwelling sheets, cold material accumulates above 670 km depth, building up until huge catastrophic breakthroughs[1,4,5] into the lower mantle are precipitated, flushing the local upper mantle contents through broad cylindrical downwellings to the core-mantle boundary (CMB). These events occur in a globally asynchronous manner, with typically three to four in progress at any particular time. This process generates large-amplitude long-wavelength lateral heterogeneity, which may go some way towards reconciling observations of long-wavelength dominance from seismic tomography[10-15] with the much broader spectrum predicted by high-Rayleigh-number convection simulations[16,17].

The behaviour of downwellings is similar to that observed in a completely basally heated three-dimensional cartesian layer with two phase changes[18]. We find however that the use of spherical geometry and realistic internal heating greatly modifies the heat flow characteristics, geometry of lower-mantle flow, upwelling plume structure and global time-dependence, as well as aiding direct comparison with seismic tomography.

Model characteristics

Our model incorporates the effect of the endothermic transition from spinel to perovskite plus magnesiowüstite occurring at ~670 km depth, consistent with a peridotitic mantle composition[19]. Some authors have included additional phase changes in their models[2,3,5,18,48]. These slightly alter the propensity towards layering and cause some other second-order effects, but considering the other approximations and uncertainties in current mantle modelling we choose to restrict these calculations to an examination of the first-order effect due to the endothermic phase change at 670 km depth. Our preliminary modelling results with the 400 km phase change added display little qualitative difference in behaviour.

The equations of compressible self-gravitating flow are solved and integrated in time using a spectral-transform method[17], implemented on the Intel Touchstone Delta parallel supercomputer system at the California Institute of Technology. As the mantle is characterized by very high Prandtl number, inertial terms are ignored. The anelastic approximation is used, eliminating acoustic waves which propagate many orders of magnitude faster than convective velocities. Entropy, pressure, gravitational potential and poloidal mass flux potential are expanded laterally in spherical harmonics, up to degree and order 127, and the nonlinear products associated with advection and viscous dissipation are evaluated in grid space using 384 longitudinal points by 192 latitudinal points. Variables are expanded vertically in seperate Chebyshev series for the upper and lower mantles, with 33 radial levels in the lower and 17 radial levels in the upper mantle. Use of two Chebyshev expansions matched at 670 km depth gives good vertical resolution at the CMB, at 670 km depth and at the surface, where it is most needed. The fields are adequately resolved because the horizontal and vertical variances of variables fall by many orders of magnitude between maximum values and truncation[7-9,17].

As the phase boundary deflection observed in the Earth[20] is at least an order of magnitude smaller than the characteristic size of convective features in our model, it is not necessary (to a good approximation) to resolve the exact details of the phase change. Thus, deflection of the phase change resulting from

FIG. 1 Cold downwellings for final frame of simulation. Blue surface is an isocontour showing where the temperature is 110 K lower than the horizontally averaged value. Green surface is the core. A network of interconnected linear downwellings is visible in the upper mantle, with three huge cylindrical downwellings in the lower mantle, spreading out into pools of cold material above the core–mantle boundary.

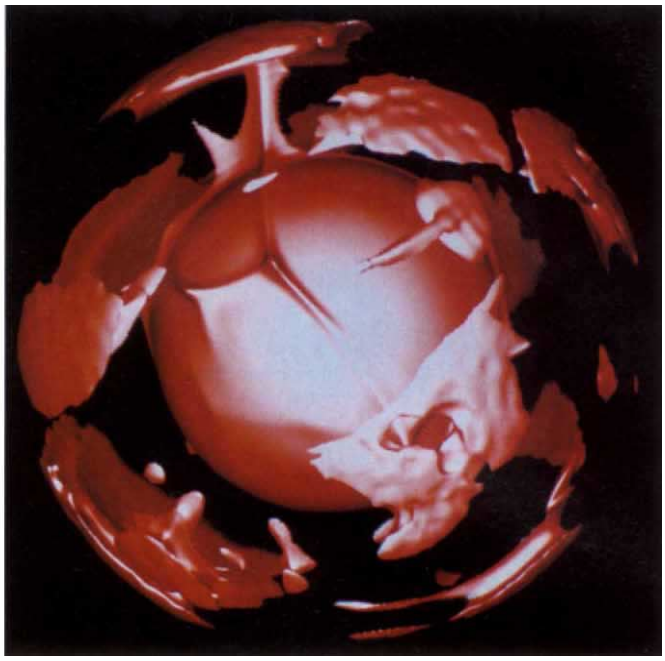

FIG. 2 Hot upwellings for final frame of simulation. Red surface is an isocontour of superadiabatic temperature, showing where the temperature is 110 K higher than the reference-state adiabat. A single plume from the core–mantle boundary feeds a hot region in the upper mantle. Note that most broad hot regions in the upper mantle are not directly linked to lower-mantle structures.

lateral temperature variations at 670 km depth is represented as a sheet mass anomaly at this depth, resulting in discontinuous normal stress between the two Chebyshev regimes. This approach has the advantage of a phase loop (the pressure or depth interval over which the multivariant phase change occurs) with zero width—important because the phase loop width affects the inhibition of flow across the boundary[5], and recent experiments[19] constrain this width to be a few kilometres at most. For numerical reasons, the latent heat release (absorption) that accompanies upward (downward) motion through the phase change must be spread out 25 km on either side of the interface. This treatment of the phase change has been validated by computing two-dimensional cartesian and spherical axisymmetric results and comparing them to previously published results[1,4].

Parameters. Entropy, pressure and gravitational potential are expanded as perturbations relative to a self-gravitating adiabatic reference state. The Murnaghan equation is assumed, leading to a polytrope[17] (that is $P \propto [\rho^{1+1/n} - \rho_0^{1+1/n}]$, where n is the polytropic index). A constant Gruneisen parameter of 1.0 and polytropic index of 0.5 gives a reasonable fit to the Earth model PREM[21]. Implicit in this treatment is the depth-dependence of material properties such as density bulk modulus and thermal expansivity, with the latter varying from 3.0×10^{-5} at the surface to 2.2×10^{-5} at 670 km depth and 1.2×10^{-5} at the CMB. Heat capacity is assumed constant at 1,250 J kg^{-1} K^{-1}. Thermal conductivity and viscosity are specified as functions of depth only, with dynamic viscosity increasing roughly exponentially from 1.7×10^{22} Pa s at the surface to 1.9×10^{22} Pa s at 670 km depth and 2.1×10^{23} Pa s at the CMB. Thermal conductivity is 2.3 W m^{-1} K^{-1} at the surface, increasing with depth as the fourth power of density, giving a lower-mantle increase consistent with experiments[22] and theory[23]. The boundary conditions at the surface and CMB are stress-free and isothermal, with the temperatures at the CMB and surface fixed at 3,450 K and 1,060 K respectively. Of the total temperature drop across the mantle, 1,250 K is superadiabatic and 1,140 K is due to adiabatic compression. The unrealistically high surface temperature is a consequence of treating the viscosity as a function of depth only rather than a function of temperature, so rheologically stiff plates are not produced. Absolute temperatures in such a calculation are not meaningful, however, except to the extent that they are adjusted to be realistic at some depth (for example, the upper mantle); only temperature differences are relevant to the convective style and vigour.

Because the ratio of internal to basal heating strongly affects the degree of layering in two-dimensional models (W. R. Peltier, personal communication), it is important to match the internal heating rate and core heat flux of the Earth as closely as possible. We therefore use an internal heating rate of 2.75×10^{-12} W kg^{-1}, compatible with chondritic values. The volume averaged Rayleigh numbers resulting from internal heating and superadiabaticity[9] are 1.8×10^7 and 1.2×10^6 respectively, an order of magnitude higher than in previous studies[7], but almost an order of magnitude less than those characterizing the Earth. Realistic Rayleigh numbers are obtainable in two-dimensional calculations[2,3,5], which are useful for predicting how the effects observed here might scale to the Earth-like regime.

We take the value of the Clapeyron slope to be -4 MPa K^{-1}, the preferred value from recent experimental results[24], although at the high end of the range from previous experiments[19]. We choose a high value so that we can determine and characterize the maximum effect that the phase change could have on the flow. Although this value has been observed to cause very strong layering in one axisymmetric result[4], the inhibiting effect of the phase change in that simulation was greatly enhanced by the use of a much lower thermal expansivity at 670 km depth than is consistent with experimental and theoretical estimates[25], and by the imposed two-dimensionality.

The simulation was started from a case with no phase change and run for about 15,000 timesteps, corresponding to about 3 billion years; the results we present here are characteristic of the last 9,000 timesteps, after the system has overcome the initial transient adjustment to the presence of the phase change.

Observables

We obtain a mean surface heat flow of 2×10^{13} W, of which

~40% comes from the core. The total is similar to that of the Earth, but the basal heatflow is considerably larger than most estimates for the Earth[26-28]. Even so, it drives very little plume activity, as discussed below. It is possible that the mantle heating rate should be substantially augmented by the effect of secular cooling[26,27,29] which is missing from the model because the heating is treated as time-independent, but this is an issue for the future.

Maximum convective velocities are ~40 mm yr^{-1} and average surface velocities typically 6 mm yr^{-1}—an order of magnitude lower than plate velocities, although a direct comparison may be misleading because our simulation lacks rigid plates. The principal difference between our parameters and the Earth probably lies in the use of higher than realistic viscosities, which is necessitated by computing limitations. At the higher Rayleigh number that would result from lower viscosities, the phase change has a stronger inhibitive effect on the flow[1,3]; thus our calculation may underpredict the degree of layering that would occur in the Earth.

Flow pattern. In Fig. 1, which illustrates cold features for the final frame of the calculation, a network of interconnected cold downwelling sheets, which do not penetrate the phase change, is observed in the upper mantle. The distance between sheets that are roughly parallel is typically 3,000–8,000 km, a scale which is consistent with present subduction zones on the Earth. They have some small-scale complexity due to local boundary-layer instabilities, which would probably be suppressed by the high-viscosity lithospheric plates on the Earth. At the intersections of these sheets, large pools of cold material form above the 670 km phase change. This cold material is gravitationally unstable and after building up sufficiently triggers a sudden avalanche into the lower mantle, in the form of a large-diameter (~1,000 km) cylindrical downwelling plume. This downwelling acts as a conduit to the CMB, effectively emptying the cold material from the local upper mantle to a large pool at the base of the mantle, despite the increase in viscosity with depth. The downwelling then shuts off completely and does not recur in exactly the same place during the simulation, although many such events may occur in the same general area, and a total of about 15 events are observed during this part of the simulation. Thus, these events cool all areas of the lower mantle and core. At any one time, several of these flushing events are in progress at different places around the sphere, triggering in a globally asynchronous manner. Owing to the spherical geometry, the surface area of the CMB is ~35% of the surface area of the 670-km interface, and thus the combined effect of flushing events occurring in different places around the sphere is to surround the core with cold material, resulting in a heat flow (40% of surface heat flow) considerably higher than most estimates for the Earth[26-29], but with very little upwelling plume activity.

Figure 2 shows the corresponding hot, upwelling regions for the final frame. The most prominent features are the broad hot regions in the upper mantle, which are generally not associated with any deep features in the lower mantle. The lateral heterogeneity is much greater in the upper mantle than in the lower mantle, as shown quantitatively below. At the CMB, ridges of hot material are observed. These are swept around by the enormous injections of cold upper mantle material caused by flushing events, and occasionally a short-lived, transient plume is formed at the intersection of these ridges, rising to the 670-km interface and injecting hot material into the upper mantle. One of these can be observed in Fig. 2. Thus, in both directions, cylindrical forms (plumes) are seen to penetrate the 670-km phase change, whereas linear forms (sheets) do not. The upward flow in the upper mantle and in the top of the lower mantle is generally the weak, distributed return flow characterizing mainly internally heated convection[7-9,30,31].

The radial dependence of the flow structure is clearly visible in Fig. 3*a* and *b*, which shows the superadiabatic temperature field in two cross-sectional slices for the final frame of the simulation. The upper mantle is extremely heterogeneous on long wavelengths, containing some broad (up to ~10,000 km) regions of anomalously cold or hot material, as well as regions with the classical small aspect-ratio convection cells[32,33]. In the lower mantle, two large cylindrical downwellings are visible (Fig. 3*b*), and a thick layer of cold material surrounds the core. One broad upwelling plume from the CMB (Fig. 3*a*) penetrates the 670-km phase change and injects hot material into the upper

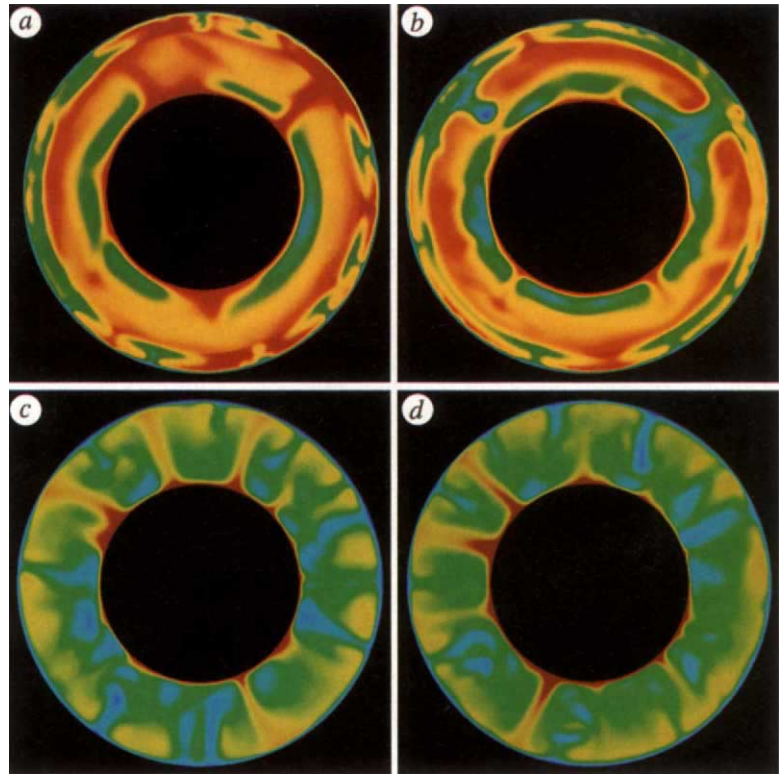

FIG. 3 Superadiabatic temperature field on different cross-sectional slices. *a* and *b*, The final frame of the phase change simulation. Scale ranges from −1,050 K to +350 K. *c* and *d*, A typical case with no phase change. This is representative of mainly internally heated whole-mantle models[7-9,30,31], with Rayleigh numbers for internal and basal heating of 1.4×10^7 and 5.5×10^5 respectively, a factor of 10 viscosity increase with depth, and a basal heat flow of ~16% of the surface heat flow. Scale ranges from −780 K to +220 K.

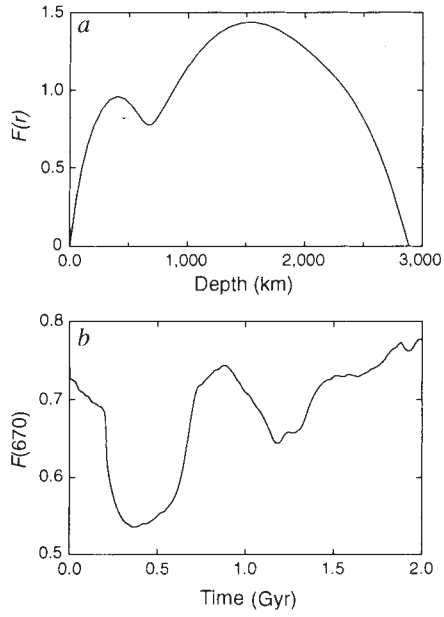

FIG. 4 *a*, Radial mass flux diagnostic $F(r)$ for the final frame of simulation. *b*, Time series of $F(670)$ for the last 9,000 timesteps (2 Gyr). $F(r)$, defined in ref. 5, is the spherically averaged modulus of radial mass flux, normalized so that the integral over non-dimensional depth is unity.

mantle, but this is the only such feature in the whole lower mantle. The inclusion of realistic temperature-dependent viscosity would result in a low-viscosity layer immediately above the CMB because of the thermal boundary layer, which may result in more upwelling plumes. The lack of strong plume activity in our model is not, however, of concern as plumes on the Earth are merely secondary features, carrying only 10–15% of the total heat flux[28].

The ability of the cold downwelling lower mantle plumes to reach the CMB, despite the increasing viscosity and decreasing thermal expansivity with depth, is in marked contrast to a similar case with no phase change illustrated in Fig. 3*c* and *d*, in which the somewhat smaller downwellings slow down and broaden in the lower half of the mantle, allowing the formation of many upwelling plumes, despite the low basal heat flux. It is possible that a larger viscosity increase with depth[28] may slow down the giant drips observed in the phase-change case. They are such large features, however, with so large a reservoir of feeding material, that it seems unlikely that they will be prevented from reaching the CMB.

Radial mass flux. A useful indicator is the radial mass flux diagnostic[5], defined as the spherically averaged absolute radial mass flux, normalized so that the integral over non-dimensional depth is unity. This diagnostic for the final frame is shown in Fig. 4, together with the time-series of mass flux through the 670-km discontinuity for the last 9,000 timesteps (~2 Gyr) of the simulation. The phase change is observed to have a marked inhibitive effect on the flow, indicated by the minimum in the radial mass flux at 670 km. Examination of this diagnostic for individual spherical harmonic degrees indicates that long wavelengths of flow are virtually unaffected by the phase change, whereas short wavelengths are increasingly inhibited; for spherical harmonic degrees above ~40, flow is effectively confined to the upper mantle.

From the radial mass flux across the interface at 670 km depth it is possible to calculate a 'mixing time', defined as the time required for a mass equal to the mass of the mantle to pass through 670 km. For this case the time is 4.5 Gyr. To scale to the Earth's Rayleigh number (Ra), it is likely that the mass flux (of downwelling cold material) scales roughly as the heat flux, suggesting a $Ra^{1/3}$ scaling[34] which would reduce the mixing time to ~2.1 Gyr for an order of magnitude increase in Ra. This is less than half the age of the Earth, but the increased effect of the phase change at higher Ra[1,3] may increase this time.

There is some time dependence of the flow through the phase change at 670 km depth, with the mass flux diagnostic at 670 km depth ($F(670)$) varying between 0.5 and 0.8 during this simulation. This time dependence is much weaker than that observed in two-dimensional geometry[4,5,48]. Owing to the large effective aspect ratio in our spherical simulation, several flushing events are typically occurring at any given time, so the convection is never strongly layered on a global scale. As a result globally averaged diagnostics such as $F(670)$, mean temperature, and so on are not greatly affected by an individual flushing event. Given the observed preference for a penetration in cylindrical rather than linear forms, it is also possible that in two-dimensional geometry (where up- or downwellings are restricted to being linear), cold material builds up to a greater extent before it can be flushed into the lower mantle, and thus these events are more violent. It is possible that our flushing events would be more abrupt and violent if we could decrease the viscosity to Earth-like values, as observed in two-dimensional models (ref. 48, and W. R. Peltier, personal communication). We believe however, that with an Earth-like viscosity, flushing events would still overlap in time, and the global time dependence would be intrinsically weaker in full three-dimensional spherical geometry than in spherical axisymmetric or two-dimensional cartesian geometries.

Spherically averaged temperature. The horizontally averaged ($l = 0$) temperature field is shown in Fig. 5. A temperature drop of several hundred degrees occurs around 670 km depth. In addition a small kink is observed at 670 km, due to the release or absorption of latent heat by material advected across the phase change. The net thermal gradient at 670 km depth is low, and thus the conductive heat flow across the 670-km interface is only ~10% of the surface heat flow, with most of the heat flux across 670 km depth being advected. On local scales, much steeper temperature gradients are observed in regions far from cyclindrical downwellings and most of the radial heat flux may be conductive.

Lateral heterogeneity and seismic tomography

The effects of the phase change on both the horizontal spectrum of density anomalies and the depth-dependence of total power[5] is pronounced, resulting in a dominance of long-wavelength power in the upper mantle and base of the lower mantle, and a concentration of total power in the same areas (Fig. 6*a* and *b*), compatible with seismic tomography[13,15]. In the upper mantle the dominant frequencies are spherical harmonic degrees $l =$ 2–7, with a peak at $l = 6$, whereas in the deepest ~400 km of the lower mantle, $l = 2$ and 3 dominate, with a secondary peak

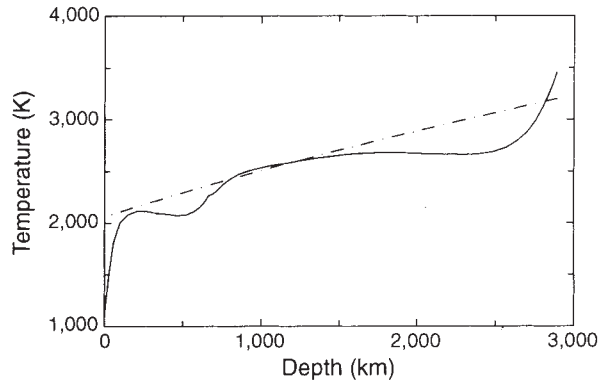

FIG. 5 Solid line, radial profile of spherically averaged temperature for final frame. Dashed line, reference state adiabat.

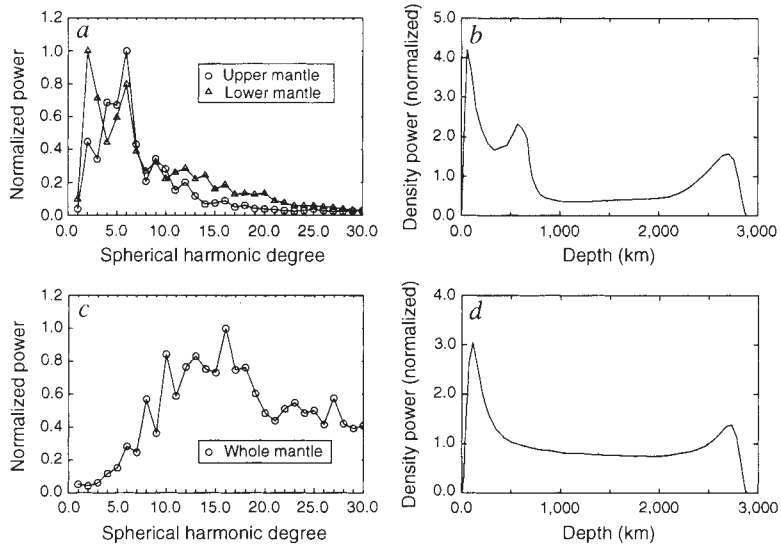

FIG. 6 *a*, Power in each spherical harmonic degree, vertically averaged through upper and lower mantles, for the final frame. This lateral power spectrum has similarities with that observed by Inoue *et al.* using seismic tomography (plotted in ref. 13, Fig. 5) *b*, Radial profile of total lateral heterogeneity (in density). A peak is observed at 670 km depth, as with two-dimensional results[5]. *c*, Power in each spherical harmonic degree, vertically averaged through the whole mantle, for the case with no phase change (illustrated in Fig. 3*c* and *d*). *d*, As *b* for the case with no phase change.

at $l = 5$–6. This is very different from the illustrated result with no phase change (Fig. 6*c* and *d*), in which a broad peak is observed in the range $l = 8$–20; and also with basally heated model at $Ra = 10^6$ (ref. 17; Fig. 1) which peaks at $l = 10$. Indeed, the lateral spectrum is fairly consistent with the observations of long-wavelength dominance from seismic tomography[10–13,15,35], particularly that of Inoue *et al.*[35] (plotted in refs 13 and 15). The flow lacks the dominant $l = 2$ component found in some seismic models[10–12]; this is probably due to the absence of tectonic plates and continents, as discussed later. The asymptotic fall-off in power with spherical harmonic degree varies with depth, but is roughly proportional to l^{-2}.

Even when filtered to seismic tomographic resolution (for example $l = 10$, Chebyshev degree $n = 13$), the effect of the phase change is still clearly discernible, both in the entropy field and in radial correlations between layers[49]. However, all plume-like upwellings on the lower mantle disappear completely. The strongest of the broad cylindrical downwellings are visible as smeared out cold anomalies, and thus may be discernible in tomographic models. The peak in the radial heterogeneity profile (Fig. 6*b*) is still visible at $n = 13$, but disappears at $n = 6$. Although the lateral heterogeneity spectrum is dominated by long wavelengths, we need to expand to at least $l \approx 31$ to see all the main features.

Slab Penetration

The issue of whether subducting lithospheric slabs penetrate the lower mantle or are deflected by the 670-km discontinuity is central to the question of mantle layering[36–42]. The closest analogues to slabs in our model are the linear downwellings in the upper mantle, and our model results suggest that slabs do not immediately penetrate, but instead build up in the transition zone until enough cold mass has accumulated to precipitate an avalanche into the lower mantle[43]. This picture would be consistent with (1) strong correlations between past locations of subduction and seismically fast ('cold') regions at the base of the upper mantle and top of the lower mantle[44], (2) recent tomography of slabs[39–41] showing that at least in some areas slabs flatten out along the 670-km discontinuity and appear to stagnate in the transition zone, (3) recent global tomography[14] showing broad seismically fast areas at 600 km depth in places where subducted slabs would be expected to accumulate, and (4) global mapping of topography on the 670-km discontinuity[20] favouring models in which subducting slabs are deflected horizontally at the discontinuity.

Differences from the Earth?

Although our model does not include the effects of variable viscosity, tectonic plates or continents, many of the chief characteristics of the Earth are reproduced, such as the predominance of linear downwellings in the upper mantle (analogous to slabs), wavelength of upper-mantle features (compatible with typical plate sizes), the secondary nature of upwelling plumes, and the similarity of lateral heterogeneity spectra at different depths with seismic tomographic models[13,15].

One difference is that junctions of linear downwellings, at which the large pools of cold material build up in our model, are not observed in the Earth except at the intersection of the Pacific, Philippine and Eurasia plates. This may make catastrophic breakthrough more difficult and more violent, as in two-dimensional models[1,4,43,48]. In addition, the cold slab material is highly viscous and if deflected by the phase change, may have a greater tendency to stagnate in the transition zone.

The addition of rigid plates would probably reinforce the long-wavelength nature of the flow[45,46]. The plate-tectonic cycle, including subduction-zone locations, may be controlled by the assembly and breakup of supercontinents[47], which would pump power into the very lowest spherical harmonic degrees[44]. □

Received 30 November 1992; accepted 29 January 1993.

1. Christensen, U. R. & Yuen, D. A. *J. geophys. Res.* **90,** 10291–10300 (1985).
2. Liu, M., Yuen, D. A., Zhao, W. & Honda, S. *Science* **252,** 1836–1839 (1991).
3. Zhao, W., Yuen, D. A. & Honda, S. *Phys. Earth planet. Inter.* **72,** 185–210 (1992).
4. Machetel, P. & Weber, P. *Nature* **350,** 55–57 (1991).
5. Peltier, W. R. & Solheim, L. P. *Geophys. Res. Lett.* **19,** 432–324 (1992).
6. Wyllie, P. J. *Rev. Geophys.* **26,** 370–404 (1988).
7. Glatzmaier, G. A., Schubert, G. & Bercovici, D. *Nature* **347,** 274–277 (1990).
8. Bercovici, D., Schubert, G. & Glatzmaier, G. A. *Science* **244,** 950–955 (1989).
9. Schubert, G., Bercovici, D. & Glatzmaier, G. A. *J. geophys. Res.* **95,** 14105–14129 (1990).
10. Nakanishi, I., & Anderson, D. L. *J. geophys. Res.* **88,** 10267–10283 (1983).
11. Tanimoto, T. *J. Phys. Earth* **38,** 493–509 (1990).
12. Tanimoto, T. *Geophys. J. Int.* **100,** 327–336 (1990).
13. Su, W. & Dziewonski, A. M. *Nature* **352,** 121–126 (1991).
14. Su, W., Woodward, R. L. & Dziewonski, A. M. *Nature* **360,** 149–152 (1992).
15. Su, W.-J. & Dziewonski, A. M. *Phys. Earth planet. Inter.* **74,** 29–54 (1992).
16. Jarvis, G. T. & Peltier, W. R. in *Mantle Convection: Plate Tectonics and Global Dynamics* (ed. Peltier, W. R.) 479–594 (Gordon and Breach, New York, 1989).
17. Glatzmaier, G. A. *Geophys. astrophys. Fluid Dyn.* **43,** 223–264 (1988).
18. Honda, S., Yuen, D. A., Balachandar, S. & Reuteler, D. *Science* (in the press).
19. Ito, E. & Takahashi, E. *J. geophys. Res.* **94,** 10637–10646 (1989).
20. Shearer, P. M. & Masters, T. G. *Nature* **355,** 791–796 (1992).
21. Dziewonski, A. M. & Anderson, D. L. *Phys. Earth planet. Inter.* **25,** 297–356 (1981).
22. Osako, M. & Ito, E. *Geophys. Res. Lett.* **18,** 239–242 (1991).
23. Anderson, D. L. *Phys. Earth planet. Inter.* **45,** 307–323 (1987).
24. Ito, E., Akaogi., M. Topor, L. & Navrotsky, A. *Science* **249,** 1275–1278 (1990).
25. Anderson, O. L., Oda, H. & Isaak, D. *Geophys. Res. Lett.* **19,** 1987–1990 (1992).
26. Schubert, G. *Ann. Rev. Earth Planet. Sci.* **7,** 289–342 (1979).
27. Schubert, G., Stevenson, D. J. & Cassen, P. *J. geophys. Res.* **85,** 2531–2538 (1980).
28. Davies, G. F. & Richards, M. A. *J. Geol.* **100,** 151–206 (1992).
29. Sharpe, H. N. & Peltier, W. R. *Geophys. Res. Lett.* **5,** 737–740 (1978).
30. Houseman, G. *Nature* **332,** 346–349 (1988).
31. Travis, B, Weinstein, S. & Olson, P. *Geophys. Res. Lett.* **17,** 243–246 (1990).
32. Christensen, U. & Yuen, D. *Geophys. Res. Lett.* **15,** 597–600 (1988).
33. Busse, F. H. in *Mantle Convection: Plate Tectonics and Global Dynamics* (ed. Peltier, W. R.) 23–95 (Gordon and Breach, New York, 1989).

34. Turcotte, D. L. & Schubert, G. *Geodynamics: Applications of Continuum Physics to Geological Problems* 279–285 (Wiley, New York, 1982).
35. Inoue, H., Fukao, Y., Tanabe, K. & Ogata, Y. *Phys. Earth planet. Inter.* **59,** 294–328 (1990).
36. Creager, K. C. & Jordan, T. H., *J. geophys. Res.* **91,** 3573–3589 (1986).
37. Vidale, J. E. & Garcia-Gonzales, D. *Geophys. Res. Lett.* **15,** 369–372 (1988).
38. Zhou, H. W. & Anderson, D. L. *Proc. natn. Acad. Sci. U.S.A.* **86,** 8602–8606 (1989).
39. Zhou, H. W. & Clayton, R. W. *J. geophys. Res.* **95,** 6829–6851 (1990).
40. van der Hilst, R., Engdahl, R., Spakman, W. & Nolet, G. *Nature* **353,** 37–43 (1991).
41. Fukao, T., Obayashi, M., Inoue, H. & Nenbau, M. *J. geophys. Res.* **97,** 4809–4822 (1992).
42. Christensen, U. R. & Yuen, D. A. *J. geophys. Res.* **89,** 4389–4402 (1984).
43. Solheim, L. P. & Peltier, W. R. *J. geophys. Res.* (in the press).
44. Scrivner, C. & Anderson, D. L. *Geophys. Res. Lett.* **19,** 1053–1056 (1992).
45. Davies, G. F. *J. geophys. Res.* **93,** 10451–10466 (1988).
46. Gurnis, M. & Zhong, S. *Geophys. Res. Lett.* **18,** 581–584 (1991).
47. Gurnis, M. *Nature* **332,** 695–699 (1988).
48. Weinstein, S. A. *Geophys. Res. Lett.* **20,** 101–104 (1993).
49. Jordan, T. H., Puster, P., Glatzmaier, G. A. & Tackley, P. J. *Nature* (submitted).

ACKNOWLEDGEMENTS. We thank W. R. Peltier, D. L. Anderson, D. A. Yuen, M. Gurnis, V. Solomatov and the participants of the Los Alamos Mantle Convection Workshop for discussions, U. Christensen for his review and H. X. Qian for photographic assistance. The Intel Touchstone Delta System was operated by the California Institute of Technology on behalf of the Concurrent Supercomputing Consortium. Access to this facility was provided by the institute. P.T. thanks the NSF for financial support.

LETTERS TO NATURE

The proper motion of Geminga's optical counterpart

G. F. Bignami*†, P. A. Caraveo* & S. Mereghetti*

* Istituto di Fisica Cosmica del CNR, Via Bassini 15, 20133 Milano, Italy
† Dipartimento di Ingegneria Industriale, Università di Cassino, Via Zamosh 43, 03043 Cassino, Italy

THE strong γ-ray source Geminga was first observed by the satellite SAS-2[1,2] and later seen by the COS-B satellite[3,4]. An association with the peculiar X-ray source 1E0630+178 was proposed[5], suggesting that Geminga is a nearby neutron star (~100 pc from Earth) which is not visible as a radio pulsar. Searches for its optical counterpart yielded as the best candidate a very faint ($m_v = 25.5$) object, G″, which was proposed on the basis of its colours[6–8]. The association of Geminga with 1E0630+178 was confirmed recently by the discovery of a 237-ms periodicity in the soft X-ray emission[9] from the latter; such oscillations were recognized immediately afterwards in data[10] from the Gamma Ray Observatory, and in reanalysis of the COS-B[11] and SAS-2 data[12]. As its timing and energy parameters indicated that Geminga is closer than 400 pc, Bignami and Caraveo suggested[11] that the proper motion of the optical counterpart G″ might be measurable. Here we compare a 1992 optical image of G″ with previous data from 1984 and 1987, and find that the proper motion is 0.17 arcsec per year. This motion is consistent with the identification of G″ as a neutron star at a distance of about 100 pc, thus confirming it as the optical counterpart of Geminga.

On 4 November 1992 an observing run in service mode was made with the New Technology Telescope (NTT) of the European Southern Observatory (ESO) on La Silla, Chile. Using the Super Seeing Imager (SUSI)[13] set up to take advantage of the very good seeing (0.6–0.8″), 10 exposures of 15′ each were taken through a Johnson V filter, with a pixel size corresponding to 0.13″. The data were reduced and summed directly on the mountain (A. Moneti, personal communication). The resulting image was compared with two others of the same field, one obtained at the Canada-France-Hawaii Telescope (CFHT) 3.5-m instrument in January 1984 (ref. 6) and the other at the ESO La Silla 3.6-m in January 1987 (ref. 8).

Figure 1 shows a composite of the three images, where the 1984 and 1987 images have been rebinned and tilted to match the scale and orientation of the NTT 1992 frame. The motion of G″ to the northeast is apparent, showing a displacement of about 12 pixels between 1984 and 1992, with the 1987 data at the correct angle and position.

To assess the effect more quantitatively, and to exclude any possible systematic error, we adopted the following procedure. The pixel positions of 16 objects of magnitude ~24–26 were measured in each of the three frames shown (partially) in Fig. 1. For each star, a mean position was calculated, and deviations from the mean are given in Fig. 2 in units of pixels (0.13″) for the x and y axes. Whereas the comparison objects seem to lie well within the centring errors in each image, G″ does not. Its total displacement of 12 pixels to the northeast, which consists of two similar components ($\Delta x \approx 10$ px, $\Delta y \approx 7$ px), indicates the high confidence level of the observed effect, especially when compared with the average <2 pixel position jitter of the comparison faint stars. Furthermore, the three positions found for G″ show a coherent pattern of movement.

The coordinates of G″ at the three epochs are: for 1992, $\alpha_{(1950)} = 6\text{ h }30\text{ min }59.15\text{ s}$, $\delta_{(1950)} = 17°\,48'\,33.6'' \pm 0.16''$; for 1987, $\alpha_{(1950)} = 6\text{ h }30\text{ min }59.10\text{ s}$, $\delta_{(1950)} = 17°\,48'\,33.0'' \pm 0.68''$; for 1984, $\alpha_{(1950)} = 6\text{ h }30\text{ min }59.06\text{ s}$, $\delta_{(1950)} = 17°\,48'\,32.7'' \pm 0.46''$. All the above coordinates have been computed in the original (not rebinned) data, using a common set of reference stars extracted from the original Hubble Space Telescope (HST) Guide Star Catalogue. The quoted uncertainties take into account the r.m.s. of the astrometry fit (0.10″, 0.12″ and 0.19″ in the 1992, 1987 and 1984 data, respectively) and the error in the centring of G″ (~1 pixel of each original data set: 0.13″, 0.675″, 0.412″ in the 1992, 1987 and 1984 images, respectively). These uncertainties only reflect the relative astrometry errors. As such, they cannot be used directly for absolute positions, because they do not take into account the absolute astrometry errors of the HST Guide Star Catalogue. A linear fit to the above coordinates gives the following components for the proper motion of G″: $\mu_\alpha = 0.14''\,\mathrm{yr}^{-1}$, $\mu_\delta = 0.10''\,\mathrm{yr}^{-1}$ for a total of $\mu = 0.17''\,\mathrm{yr}^{-1}$, to which a conservative error of $\pm 0.05''\,\mathrm{yr}^{-1}$ should be attached.

The large proper motion of G″ ($m_v = 25.5$) can only be interpreted in two ways: either the object is a Solar System body (for example an asteroid or comet), or it is a subluminous, truly faint star. The first possibility cannot be discarded lightly, in view of the low ecliptic latitude of Geminga. Two strong arguments against it, however, are the extremely slow motion (for a Solar System body) at a large angle with the ecliptic plane, and the low probability of the event, in view of the small area considered. Proof, in the end, will come from observing the proper motion of the X-ray source, the reference for which is the Einstein Observatory's High Resolution Imager (HRI) 1981 position. Comparison with the Rosat satellite's HRI 1991 position might be interesting but unlikely to be conclusive. Interpreting G″ as a star, the convenient relation $\mu = 0.2 v_{100} d_{100}^{-1}$ applies, where μ is in arcsec per year, v_{100} is the object velocity in the plane of the sky in units of 100 km s^{-1}, and d_{100} its distance in units of 100 pc. For a displacement similar to that observed, this gives a distance of the order of 100 pc for a velocity in the plane of the sky of 100 km s^{-1}, not far from the mean for the broad velocity distribution of radio pulsars[14]. At 100 pc, for example, the object would have a visible magnitude $M_v = 20.5$. This should be compared, for example, with $M_v = 15$ for the Vela pulsar; that is, it has an underluminosity only comprehensible for a neutron star. Anything more luminous would have to be correspondingly more distant and thus faster. For comparison, the Vela pulsar, at an accepted distance of 450 pc, has been measured[15] to have a proper motion of about $0.05''\,\mathrm{yr}^{-1}$. The only normal stars that could in principle mimic the magnitude and velocity of G″ are the 'late-type extreme subdwarfs', characterized by large transverse velocities, red colours and absolute